Applied Thermal Engineering 188 (2021) 116530

Contents lists available at ScienceDirect

Applied Thermal Engineering

journal homepage: www.elsevier.com/locate/apthermeng

# Performance analysis and multi-objective optimization for tubes partially filled with gradient porous media

Chunyu Shi, Miaozhi Wang, Jun Yang, Wei Liu, Zhichun Liu *

*School of Energy and Power Engineering, Huazhong University of Science and Technology, Wuhan 430074, China*

ARTICLE INFO

*Keywords:*
Gradient porous media
Multi-objective optimization
Heat transfer enhancement
Numerical simulation

ABSTRACT

Based on the excellent performance of porous media and the popularity of additive manufacturing technology, gradient porous media with unique properties are gradually applied in the increasing fields. In this paper, the flow and heat transfer characteristics for fully developed flow in a tube partially filled with gradient porous media are investigated by numerical simulation, where the pore-size ($dp$) and porosity ($\varepsilon$) vary linearly along the radius. Keeping average pore-size $dp_a = 0.007$ m and average porosity $\varepsilon_a = 0.875$, the comparison of four configurations, classified by the pore-size and porosity distributions in the radial direction, is performed to investigate the difference in flow and heat transfer performance. Subsequently, the parametric analysis under the different filling ratios is conducted to learn the combined effect of the gradients of porosity and pore-size. The results show that the configurations with pore-size decreasing in radial direction have a better heat transfer performance where the effect of porosity arrangement on the flow and heat transfer can be neglected. As the filling ratio increasing, the performance is more sensitive to the variation of the gradients. Furthermore, a multi-objective genetic optimization coupled Kriging surrogate model is conducted with the consideration of maximum Nusselt number $Nu$ and minimum friction factor $f$ as objectives. The distribution of design variables corresponding to the optimal configurations is obtained by weighing two optimization objectives. The optimal results show that the flow resistance can be reduced by up to 19.573%, and the heat transfer efficiency can be increased by up to 7.088% compared with the homogeneous porous media under the filling ratio $r_d = 0.7$.

## 1. Introduction

Nowadays the problem of energy shortage is becoming increasingly serious, the development of new energy and the research of energy conservation technology has aroused widespread concern. Heat transfer enhancement technology is an effective approach to relieve the energy shortage, which is significant to reduce equipment investment and improve energy efficiency [1]. The conventional methods of heat transfer enhancement mainly include special-shaped structures [2–4], extended surfaces [5,6], and various inserts [7–10]. Among them, inserts are especially suitable for energy-saving retrofits of heat exchangers with the advantages of simple operation, convenient maintenance, and low investment cost.

The porous medium is a material composed of a solid matrix and internal pores, which has many superior properties compared to solid materials. Firstly, the presence of pores can retain and capture solid particles in the fluid, so the porous medium can filter gases or liquids and is an ideal material for the preparation of filters, which is widely used in water purification and vehicle emission control [11]. Secondly, mechanical and acoustic waves are reflected and refracted in the internal aperture many times, which can play the role of sound insulation, heat insulation, shock absorption, etc. Therefore, the porous medium has excellent energy-absorbing properties, which is widely used in fire prevention, noise control, and collision protection in building and automobile manufacturing [12,13]. In the chemical industry, the porous medium is widely used as a catalyst carrier with its large specific surface area, high strength, and corrosion resistance. In the healthcare industry, the harmlessness and good compatibility of porous titanium materials make them suitable for orthopedic joint correction and dental implants. In addition to the applications in these fields, porous media also have many important applications in thermal management systems [14–16]. The energy storage efficiency can be improved by embedding porous media into phase change materials. And the performance of proton exchange membrane fuel cells [17], CPUs [18], photovoltaic modules [19], and thermo-electric waste heat recovery systems [20,21] can be enhanced by intensifying the heat transfer through the use of porous media.

* Corresponding author.
*E-mail address:* zcliu@hust.edu.cn (Z. Liu).

https://doi.org/10.1016/j.applthermaleng.2020.116530
Received 26 September 2020; Received in revised form 25 November 2020; Accepted 30 December 2020
Available online 21 January 2021

**Nomenclature**

| | |
|---|---|
| $F$ | inertia coefficient |
| $f$ | friction factor |
| $h$ | heat transfer coefficient |
| $K$ | permeability of porous media($m^2$) |
| $L$ | length of computational zone(m) |
| $L_0$ | length of porous inserts(m) |
| $Nu$ | Nusselt number |
| $Q_w$ | heat flux applied to tube($W{\cdot}m^{-2}$) |
| $Re$ | Reynolds number |
| $r_0$ | radius of tube(m) |
| $r_d$ | filling ration |
| $rp$ | radius of porous inserts(m) |
| $T_{in}$ | inlet temperature of fluid(K) |
| $T_m$ | bulk temperature(K) |
| $T_w$ | wall temperature(K) |
| $U$ | dimensionless velocity |
| $u_{in}$ | inlet velocity of fluid($m{\cdot}s^{-1}$) |

*Greek symbols*

| | |
|---|---|
| $\varepsilon$ | porosity |
| $\theta$ | dimensionless temperature |
| $\lambda$ | thermal conductivity($W{\cdot}m^{-1}{\cdot}K^{-1}$) |
| $\Delta\varepsilon$ | difference of porosity |
| $\Delta dp$ | difference of pore-size(m) |
| $\Delta p$ | pressure drop(Pa) |

*Subscripts*

| | |
|---|---|
| $a$ | average value |
| $e$ | effective |
| $f$ | fluid phase |
| $s$ | porous matrix |

In the study of heat transfer enhancement, the porous medium is also considered as an excellent insert because it can improve the effective thermal conductivity of the fluid and increase the surface contact area. Porous inserts have been implemented in different thermal systems and numerous studies have been conducted with different shape designs, material properties, and insert positions. Tubes are the basic components of all kinds of thermal equipment, so the heat transfer enhancement by inserting porous media into tubes has attracted the attention of many researchers. Mohamad [22] compared thermo-hydrodynamic performance in tubes with fully filling and partially filling porous media. He observed that partially filling can increase the rate of heat transfer with a reasonable pressure drop, and the optimum radius ratio is about 0.6. Mahjoob and Vafai [23] investigated the effects of porous media microstructural properties on the heat exchanger performance and found that a higher heat transfer and pressure drop can be achieved by decreasing the pore size or porosity. Yang and Hwang [24] presented the results of numerical simulations to investigate the turbulent heat transfer enhancement in the pipe filled with porous media, the parametric studies covering Reynolds number, Darcy number, and the porous radius ratio were performed additionally. Huang et al. [25] further conducted both experimental and numerical studies to discuss the integrated impact of the porous insert on heat transfer enhancement by the performance evaluation criteria (PEC). The results showed that the porosity corresponding to the optimal PEC value is different when the flow changes from laminar to turbulent. Teamah et al [26] performed numerical simulation on two shapes of porous inserts respectively. The fluid transport in the porous region was describing. Ge et al [27] coupled computational fluid dynamics (CFD) and multi-objective genetic algorithm to optimize the configurations of porous inserts and the best configuration of porous inserts was obtained by technique for order preference by similarity to an ideal solution (TOPSIS). Siavashi et al [28] numerically studied the effect of porous layer thicknesses and positions based on the second laws of thermodynamics and then the effect of porous rib arrays on the heat transfer was investigated [29].

Additionally, some researchers focused their views on the heat transfer in the microchannels with porous inserts. Huang and Chen [30] performed a numerical simulation to investigate the effect of porous-covering block on the cooling of the block heater and found that the heat transfer rate increases with the dimensionless height of the porous cover. Hung et al [31–34] numerically studied the hydraulic and thermal performance of porous inserts with different configuration designs and found that the lowest pressure drop was observed for a sandwich distribution design. Based on the fact that the Y-shaped porous inserts have excellent thermal performance, Shen et al [35] proposed a novel design of porous inserts combined with Y-shaped porous blocks and porous layers attached to the wall. The research indicated that the proposed shape has better overall thermal performance because it possesses the advantages of mixing fluid flow caused by the Y-shaped porous insert and the thin porous layer.

A double-pipe heat exchanger is also a common arrangement in the industry and it is also necessary to study the impact of inserting porous media to strengthen the heat transfer in double-pipe exchangers. Du et al [36] applied the two-equation model to investigate conjugated heat transfer in the double pipe heat exchanger filled with porous media and the optimal filling range of porous media was determined. Targui and Kahalerras [37] inserted porous baffles into double-pipe exchangers for improving thermal performances and the impact of the permeability of porous baffles on the flow field and heat transfer efficiency is analyzed. Shirvan et al [38,39] numerically investigated the heat exchanger effectiveness enhancement in a double pipe exchanger filled with porous media and the sensitivity analysis was performed to obtain the effects of the three parameters of Reynold number, Darcy number, and the porous layer thickness on the heat transfer efficiency. Alhusseny [40] installed the porous media in the form of guiding vanes to construct a secondary flow for improving the heat transfer performance of double pipe exchangers. Siavashi and Miri Joibary [41] employed porous layers with different Darcy numbers to investigate the proper porous layer thickness and Darcy number for obtaining the maximum PEC value in a double pipe exchanger and found that there are three optimal situations to maximize the PEC. Miri Joibary and Siavashi [42] focused their research on the coupling of Re asymmetry and porous media properties used in the inner and outer pipe of the double pipe exchanger to obtain a better thermal performance and they found that there exists an optimal Re to maximize the PEC value when both pipes are filled with porous media.

The intensify of heat transfer over the cylinder caused by the arrangement of porous media is also a hot issue. Al-Salem [43] investigated experimentally the effects of porosity and thickness of porous sheets over a circular tube on heat transfer enhancement and found that the Nusselt number is adversely proportional to the thickness of the porous layer. Rasad et al [44] studied the steady mixed convection boundary-layer with the insertion of porous media into a stream flowing vertically upward through a cylinder. Siavashi and Iranmehr [45] proposed a wedge-shaped porous media to improve the external flow structure over the cylinder and the optimal porous region length is determined.

Natural convection enhancement by filling porous media in enclosures is another common subject in the industry. Siavashi et al [46] performed their simulation to investigate the effect of the number and length of porous fins on the heat transfer performance and analyzed the entropy generation variation with the number of fins. Ghasemi and

Siavashi [47] investigated the natural convection of the nanofluid in an enclosure filled with porous media and revealed that the porous-fluid thermal conductivity ratio plays a significant role in heat transfer and entropy generation.

Additive manufacturing technology, also known as 3D printing, is a manufacturing technology based on the discrete-cumulative principle that uses a layer-by-layer additive manufacturing method to prepare structural parts [48]. With the rapid development of additive manufacturing technology, it provides a preparation guarantee for the arbitrary structures of porous materials, and the excellent performance of non-homogeneous porous materials has attracted the attention of scholars all over the world. Yang et al [49] applied the gradient metal foam into the phase change materials for increasing the phase change rate. The temperature field and evolution of melting front with the positive and negative gradients for metal foams were compared with the uniform metal foam and the results showed that both the positive and negative gradients porosity obtain a better temperature uniformity compared with the uniform arrangement. Asiaei et al [50] researched the mixed convection of nanofluid inside an enclosure filled with multi-layer porous foam and the proper arrangement for the maximum heat transfer rate is obtained. Maghsoudi and Siavashi [51] optimized the pore sizes of porous media in varying regions to improve the mixed convection of nanofluid and the optimal pore sizes are obtained by the pattern search optimization algorithm. The results showed that the optimized arrangement could achieve an 8.3 percent improvement in heat transfer performance. Tahmasbi et al [52] performed an optimization for the multi-block porous foam to enhance the heat transfer rate and a maximum 20.4% improvement was obtained by determining the pore sizes in different porous blocks. Zheng et al. [53] divided the flow region in a circular tube into several layers along the radial direction and each layer is filled with porous media with different porosity. They found that the optimum PEC of the enhanced tube is related to the number of layers of porous inserts and as the number of layers increases, the thermal-hydraulic performance can be improved continuously. Wang et al. [54,55] analyzed the thermal and fluid flow performance of pipes filled with gradient porous media (GPM). The impacts of the gradient configurations, both in the axial and radial directions were discussed successively. The results showed that the gradient in the radial direction has a greater improvement on heat transfer and fluid flow performance than the gradient in the axial direction. Siavashi et al. [56] carried out numerical investigations of the hydraulic and thermal performance in tubes filled with gradient porous media and multi-layered porous media (GPM and MLPM). The results showed that the performances are very close between the porous materials with linear increasing porosity and stepwise increasing porosity. The optimal MLPM configuration was found by the particle swarm optimization (PSO) algorithm.

The above literature review shows that gradient porous media have better properties than the uniform porous media, although uniform porous media have been able to improve the heat transfer efficiency by their high thermal conductivity and large surface area ratio. And the gradients of the pore-size and porosity have a great influence on the heat transfer and flow performance for gradient porous media. However, the effect of the porosity gradient on the performance is studied separately from pore-size gradients in the existing literature, and the combined effect of the two gradients is worthy of further investigation. Simultaneously, in the optimization of the gradient porous media, the single objective optimization for maximizing the heat transfer rate is often used. In fact, the intensification of heat transfer often causes an increase in flow resistance. How to design the gradient configuration to minimize the flow resistance with a given heat transfer requirement is often considered in engineering.

The main purpose of this paper is to investigate the performance of flow and heat transfer in tubes filled with gradient porous media when the gradients of pore size and porosity change simultaneously. The configurations with an opposite variation of porosity and pore-size in the radial direction are also investigated. Parametric analysis and multi-objective optimization are performed to obtain the parameter distribution corresponding to the optimal performance. Although the original aim of this study is the optimization of gradient porous media in tubes for better performance, the optimization methods employed in this study can be applied to a variety of thermal systems. And the results can be used to guide the gradient arrangements of the porous media in other thermal devices, such as improving the heat transfer in microchannels, increasing the thermal efficiency of Stirling engines, reducing the solar energy losses in parabolic trough collector plants, and increasing the output power of proton exchange membrane fuel cells. The availability of the Pareto solution facilitates engineers to determine the porous configurations, which allows them to get the ideal solution by weighting their needs.

## 2. Computational model and numerical method

### 2.1. Physical description of the problem

The physical problem studied in this paper is illustrated in Fig. 1. A 2-D, axisymmetric numerical model for heat transfer of fully developed flow in a tube with uniform heat flux, $Q_w = 200$ W/m$^2$, is considered. The total length and radius of the computational domain are $L = 3$ m and $r_0 = 0.1$ m, respectively. Here, the core flow of the pipe is filled with GPM with the filling radius $rp$ and the filling length $L_0 = 2$ m. The pore-size ($dp$) and porosity ($\varepsilon$) of GPM change linearly with the specific gradient along the radius. Different pore-size and porosity gradients correspond to different microstructures of GPM, but the averages of the gradients remain unchanged. As shown in Fig. 2, keeping average pore size $dp_a = 0.007$ m and average porosity $\varepsilon_a = 0.0875$, the microstructure of GPM can be determined by the $\Delta dp$ and $\Delta\varepsilon$, which can be written as:

$$\Delta dp = dp_r - dp_0, \quad \Delta\varepsilon = \varepsilon_r - \varepsilon_0 \tag{1}$$

Where $dp_0$ and $dp_r$ are the pore-size respectively at the axis of the pipe and the outmost porous insert $r = rp$. $\varepsilon_0$ and $\varepsilon_r$ are the porosity respectively at the axis of the pipe and the outmost porous insert $r = rp$.

The hydrodynamic entry section of the pipe is omitted and the fluid flows into the pipe with a parabolic entry velocity. Air is used as the working fluid and GPM is comprised of AISI304, the properties of the fluid and solid phase are listed in Table 1. To simplify the numerical calculation, the assumptions are mainly summarized below: (1) Airflow is regarded as incompressible, steady, and laminar flow. (2) The GPM is fully saturated with fluid and local thermodynamic equilibrium between the solid phase and the fluid phase is considered in the GPM. (3) The fluid and solid matrix have constant thermophysical properties. (4) Gravity effect and radiation heat transfer are considered negligible.

### 2.2. Mathematical formulation

The Forchheimer-Brinkman extended Darcy model is used to describe the flow in the porous region. The governing equations for continuity, momentum, and energy can be written as [57]:

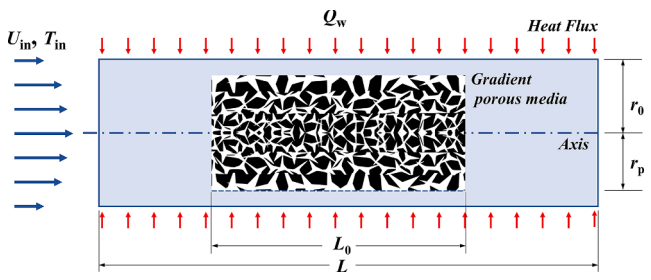


**Fig. 1.** Schematic description of the computational domain and boundary conditions.

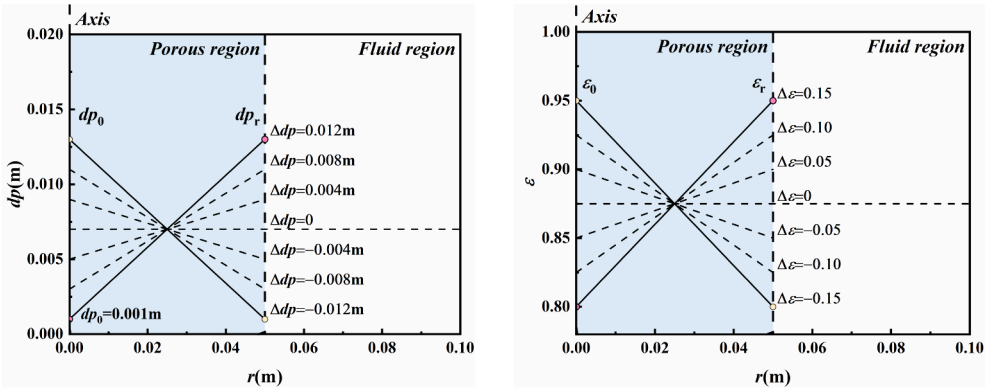


(a) the pore-size arrangements of GPMs (b) the porosity arrangement of GPMs

**Fig. 2.** the arrangements of gradient pore-size and porosity of GPMs.

**Table 1**
Thermal properties of Air and AISI304.

| Materials | $\rho$(kg m$^{-3}$) | $c_p$(J kg$^{-1}$ K$^{-1}$) | $\lambda$(W m$^{-1}$ K$^{-1}$) | $\mu$(kg m$^{-1}$ s$^{-1}$) |
|---|---|---|---|---|
| Air | 1.24 | 1006.43 | 0.027 | $1.9 \times 10^{-5}$ |
| AISI304 | 7900 | 485 | 15.2 | – |

Continuity equation:

$$\frac{\partial(\rho u)}{\partial x}+\frac{1}{r}\frac{\partial(r\rho v)}{\partial r}=0 \tag{2}$$

Momentum equations:
*x*-direction:

$$\begin{aligned}&\frac{\partial}{\partial x}\left(\frac{\rho}{\varepsilon^2}uu\right)+\frac{1}{r}\frac{\partial}{\partial r}\left(r\frac{\rho}{\varepsilon^2}vu\right)\\&=-\frac{\partial p}{\partial x}+\frac{\partial}{\partial x}\left(\frac{\mu}{\varepsilon}\frac{\partial u}{\partial x}\right)+\frac{1}{r}\frac{\partial}{\partial r}\left(r\frac{\mu}{\varepsilon}\frac{\partial u}{\partial r}\right)-\delta\frac{\mu u}{K}-\delta\frac{\rho F}{\sqrt{K}}\sqrt{u^2+v^2}u\end{aligned} \tag{3}$$

*r*-direction:

$$\begin{aligned}&\frac{\partial}{\partial r}\left(\frac{\rho}{\varepsilon^2}uv\right)+\frac{1}{r}\frac{\partial}{\partial r}\left(r\frac{\rho}{\varepsilon^2}vv\right)\\&=-\frac{\partial p}{\partial r}+\frac{\partial}{\partial x}\left(\frac{\mu}{\varepsilon}\frac{\partial v}{\partial x}\right)+\frac{1}{r}\frac{\partial}{\partial r}\left(r\frac{\mu}{\varepsilon}\frac{\partial v}{\partial r}\right)-\delta\frac{\mu v}{K}-\delta\frac{\rho F}{\sqrt{K}}\sqrt{u^2+v^2}v-\frac{\mu v}{\varepsilon r^2}\end{aligned} \tag{4}$$

Energy equation:

$$\begin{aligned}&\frac{\partial}{\partial x}\left(\rho c_p uT\right)+\frac{1}{r}\frac{\partial}{\partial r}\left(\rho c_p rvT\right)\\&=\frac{\partial}{\partial x}\left\{\left[\delta(\lambda_e-\lambda)+\lambda\right]\frac{\partial T}{\partial x}\right\}+\frac{1}{r}\frac{\partial}{\partial r}\left\{r\left[\delta(\lambda_e-\lambda)+\lambda\right]\frac{\partial T}{\partial r}\right\}\end{aligned}$$

Where $\delta$ is a parameter that is set to zero or unity when the equation applies to the fluid region or porous region, $K$ and $F$ are the permeability and inertia coefficient respectively, the calculations are given by Ergun [58]:

$$K=\frac{dp^2\varepsilon^3}{150(1-\varepsilon)^2} \tag{6}$$

$$F=\frac{1.75(1-\varepsilon)}{\varepsilon^3 dp} \tag{7}$$

$\lambda_e$ is the effective thermal conductivity of the porous media [59],

$\lambda_e=\varepsilon\lambda_f+(1-\varepsilon)\lambda_s$

As shown in Fig. 1, the boundary conditions are specified as follows:

(1) Inlet boundary

$$x=0,\quad u(r)=u_{in}\left[1-\left(\frac{r}{r_0}\right)^2\right],\quad v=0,\quad T(r)=T_{in}+\frac{qr_0}{\lambda_f}+\left[\left(\frac{r}{r_0}\right)^2-\frac{1}{4}\left(\frac{r}{r_0}\right)^4\right] \tag{9}$$

(2) Outlet boundary

$$x=L,\quad p=0 \tag{10}$$

(3) Non-slip wall boundary

$$r=r_0,\quad u=0,\quad v=0,\quad \frac{\partial T}{\partial r}=-\frac{Q_w}{\lambda_f} \tag{11}$$

(4) Axisymmetric boundary

$$r=0,\quad \frac{\partial u}{\partial r}=0,\quad v=0,\quad \frac{\partial T}{\partial r}=0 \tag{12}$$

(5) Fluid-porous interface boundary

$$r=r_p,\quad T_f=T_s,\quad -\lambda_f\nabla T_f|_n=-\lambda_s\nabla T_s|_n \tag{13}$$

### 2.3. Solution methods

In this study, the governing equations are numerically solved based on the finite volume method by the commercial CFD software, ANSYS Fluent 18.0[60]. The second upwind scheme is employed to discretize the convective terms of the governing equations. The pressure-velocity coupling field is obtained by the Semi-implicit technique for pressure-linked equations (SIMPLE) algorithm. The gradients of porosity and pore-size are realized by interpreting the User Defined Function (UDF). The solution process is terminated and considered to be converged when the standardized residuals for the continuum equations, momentum equations, and energy equations are less than $10^{-6}$, $10^{-6}$, and $10^{-8}$, respectively.

### 2.4. Data reduction

The velocity and temperature field can be obtained by numerical analysis. The friction factor ($f$) is selected as indicator to evaluate the hydraulic performance, which can be calculated from:

$$f=\frac{\Delta p}{L_0}\frac{2r_0}{(1/2)\rho_f u_{in}^2}$$

The corresponding Reynolds numbers (*Re*) is

$$Re = \frac{2\rho_f u_{in} r_0}{\mu_f}$$

The Nusselt number (*Nu*) and dimensionless temperature are employed to characterize the thermal performance, which can be calculated as

$$Nu = \frac{2hr_0}{\lambda_f} \tag{16}$$

Where $h$ is the heat transfer coefficient, it is related to the bulk temperature of air inside the pipe, $T_m$, which can be calculated as:

$$h = \frac{q}{T_w - T_m} \tag{17}$$

$$T_m = \frac{\int_0^{r_0} uTrdr}{\int_0^{r_0} urdr} \tag{18}$$

Dimensionless temperature can be express as:

$$\theta = \frac{T_w - T}{T_w - T_m} \tag{19}$$

PEC is employed to evaluate the comprehensive performance of the heat transfer and flow resistance:

$$PEC = \frac{Nu/Nu_{smooth}}{(f/f_{smooth})^{1/3}} \tag{20}$$

### 2.5. Grid independence and model validation

To ensure the accuracy of the numerical solution while improving the computational speed, the quadrilateral mapped mesh is employed which is refined near the wall with a high temperature and velocity gradient. Four different grid systems are generated to check the grid independence namely 30 × 500, 50 × 1000, 80 × 1700, 100 × 2000 in radial and axial directions. The deviation of the *Nu* number value is less than 0.05% when the number of grids exceeds 80 × 1700. Therefore, to save computational time, a mesh size of 80 × 1700 is selected for the simulations in this study.

Numerical validations are conducted according to the experimental

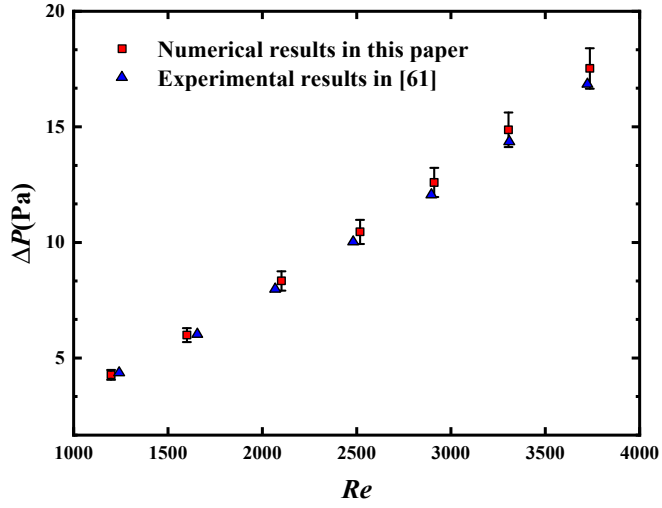


(a) Comparison of $\Delta p$ in present numerical results with experimental data

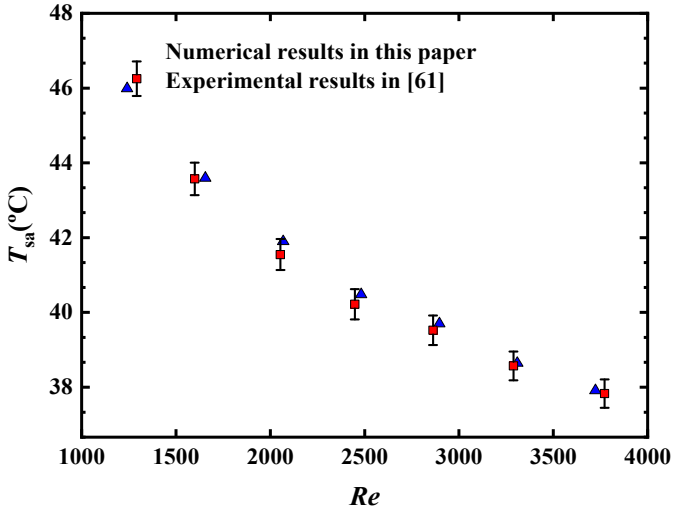


(b) Comparison of $T_{sa}$ in present numerical results with experimental data

**Fig. 3.** Comparisons of present numerical results and experimental data obtained by literature [61].

data given in the literature [61]. Under the same working conditions, the wall temperature and pressure drop are selected as comparison parameters. The numerical solutions are compared with the experimental results as shown in Fig. 3. It can be seen that the numerical solutions are in good agreement with the experimental results, which proves that the numerical method used in this paper is accurate and effective.

## 3. Performance analysis and comparison

### 3.1. Four GPM configurations comparison with HPM

With the same average pore-size $dp_a = 0.007$ m and average porosity $\varepsilon_a = 0.875$, the configuration of GPM is identified by a given $\Delta dp$ and $\Delta\varepsilon$. According to the combination of different arrangements of $\Delta dp$ and $\Delta\varepsilon$, the configurations of GPM can be divided into four types, namely pore size decreasing with porosity decreasing (PDSD), pore size decreasing with porosity increasing (PDSI), pore size increasing with porosity decreasing (PISD), pore size increasing with porosity increasing (PISI). In particular, the pore-size and porosity of HPM are as $\Delta dp = 0$ and $\Delta\varepsilon = 0$.

Fig. 4 shows the comparison of friction factor with the increase of *Re* under various porous configurations with the constant filling radius *rp* = 0.05 m. As can be seen from Fig. 4, the trends of friction factor are similar with various porous configurations, and the discrepancies become smaller with the increasing *Re*. Especially, there is no considerable difference between PISD and HPM. That is probably caused by the effect of the decrease in porosity being offset by increased pore-size. Moreover, the flow resistance of PISI is significantly lower than that of others with the same *Re*.

The effect of the gradient arrangement on the thermal performance is investigated as shown in Fig. 5. It can be seen that the thermal performances of all configurations increase as *Re* increases, but the improvement of PDSI and PDSD is inconsiderable. And the differences in the thermal performance are more obvious compared to the hydraulic performance of GPM. However, similar to the friction factors, the difference of the Nusselt number between PISD and HPM is not sufficiently significant. Within the various configurations, the case of PDSD has the best heat transfer performance.

Fig. 6 shows the variations in PEC with *Re* number under different configurations. The higher PEC value is, the more excellent comprehensive performance of GPM is. The PEC values of the different configurations all increase and then decrease as *Re* increases gradually. This is attributed to the fast growth of the *Nu* in the low *Re* conditions, but the slower growth in the high *Re* conditions. The PEC value of PISI is much lower than the others because of the much lower *Nu* with the variation of *Re* from 250 to 2000. Meanwhile, the PEC under the configuration of PDSD is the highest and has the smallest variation in the limited range of Re number which is related to the variation of the *Nu* under the configuration.

Fig. 7 shows the velocity profiles along the radius direction for different configurations. Due to the resistance caused by porous inserts, part of the air is expelled to the clear fluid region between the porous media and the pipe wall, which makes the air velocity near the wall

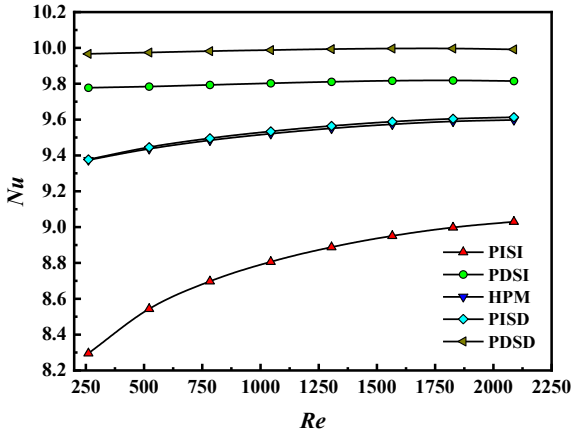


**Fig. 5.** Variations in Nusselt number with Reynolds number under four configurations of GPM.

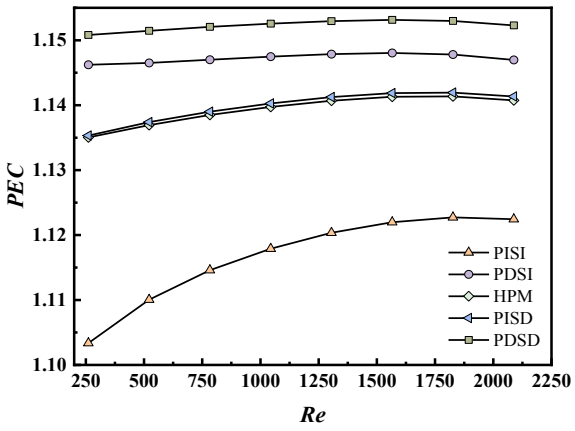


**Fig. 6.** Variations in PEC with Reynolds number under four configurations of GPM.

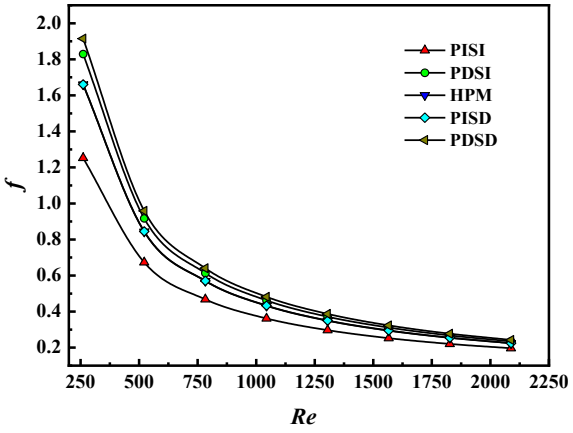


**Fig. 4.** Variations in friction factor with Reynolds number under four configurations of GPM.

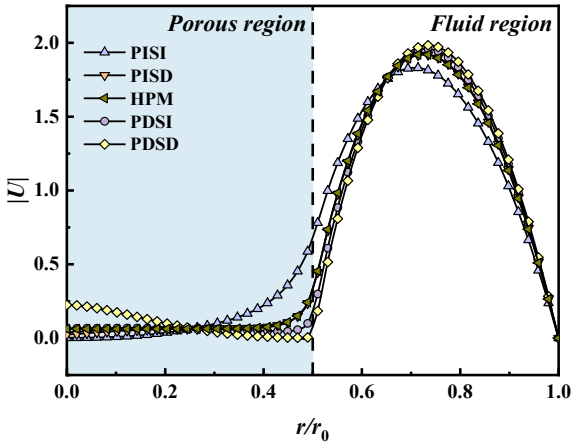


**Fig. 7.** Fully developed velocity profiles along the radius direction of GPM and HPM with *rp/r0* = 0.5 at *Re* = 1305.

increase greatly. The velocity profile will be affected when the pore-size and porosity are arranged differently. And the influence is also different between the clear fluid region and the porous region. Firstly, the configurations of the gradient directly affect the flow in the porous region. In the case of PISI, $dp$ and $\varepsilon$ increase in the radial direction together, which causes greater flow resistance near the axis and smaller in the porous-fluid interface. As a result, the velocity increase continuously along the radius in the porous region. In the case of PDSD, the simultaneous reduction of $dp$ and $\varepsilon$ results in the velocity in the porous-fluid interface approaching zero. In the cases of PDSI and PISD, the effects of changes of $dp$ and $\varepsilon$ are mutually offset, which causes the velocity variation interval of PDSI and PISD to be smaller than PDSD and PISI. Moreover, the velocity distributions of PISD and HPM are approximately coincident, which explains why the hydraulic performance of the two configurations is relatively similar. In the clear fluid region, due to the smaller flow resistance of PISI in the porous region, the maximum velocity of PISI is lower than that of other configurations.

Fig. 8 shows the dimensionless temperature distribution in the fully developed section. For the region with porous media, the equivalent thermal conductivity is significantly greater than that of air, so the dimensionless distribution has a tiny variation in that region. In the region without porous media, the temperature changes significantly with a higher temperature gradient. The insertion of porous media is similar to constructing an equivalent temperature boundary layer. It can be seen from the partially enlarged view that in the porous region, the temperature gradient under different configurations are all close to zero, and the temperature of PISI is higher than other layouts while of PDSD is the lowest. In the porous-fluid interface, the temperature gradient of the PISI is the smallest, as a result, the temperature of PISI is lower than others in most areas of the fluid region. The varied range of temperature of PDSI and PISD is between PDSD and PISI, and the temperature of PISD and HPM is also approximately coincident, which explains the similarity in heat transfer performance.

### 3.2. Parameter study on the effect of the gradient of GPM

To further understand the impacts of $\Delta dp$ and $\Delta\varepsilon$ on heat transfer and flow performance, a parameter analysis is performed by controlling other parameters remain fixed and only change the $\Delta dp$ and $\Delta\varepsilon$ of GPM, which the ranges of variations are respectively $(-0.012, 0.012)$ and $(-0.15, 0.15)$. As shown in Fig. 9 and Fig. 10, the increases in $\Delta dp$ and $\Delta\varepsilon$ reduce the flow resistance in the pipe, which simultaneously reduce the heat transfer performance. And the variations of the $f$ and $Nu$ are relatively uniform with the increasing $\Delta dp$ within the range of $\Delta dp > 0$, while within the range of $\Delta dp < 0$, the change becomes nonuniformity. The larger $\Delta dp$ is, the more obvious decrease caused by the increasing $\Delta\varepsilon$ is. It can be found also that the variations with $\Delta\varepsilon$ is approximately linear in the range of $\Delta\varepsilon < 0$, and the variation degree has increased significantly in the range of $\Delta\varepsilon > 0$.

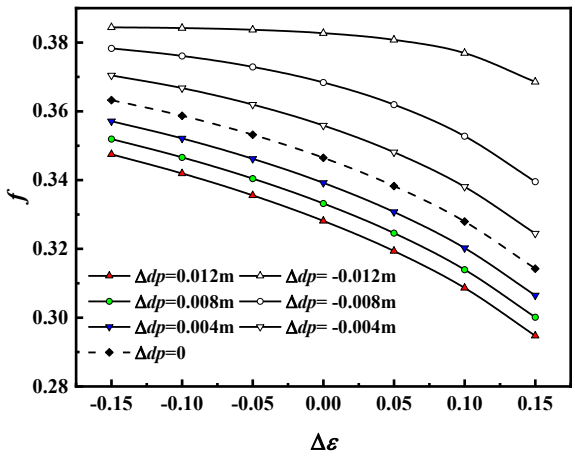


**Fig. 9.** Variations in friction factor with $\Delta dp$ and $\Delta\varepsilon$ under $rp = 0.05$ m at $Re = 1305$.

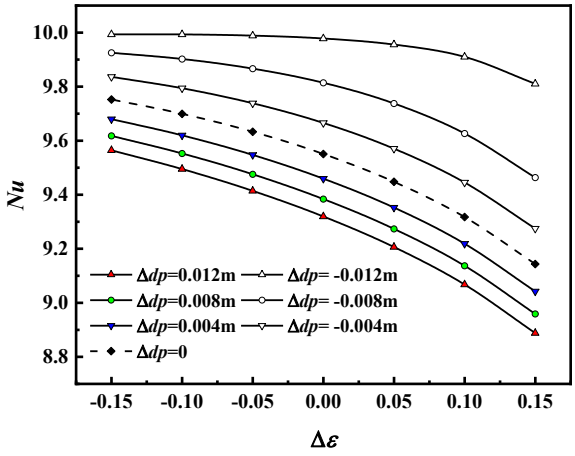


**Fig. 10.** Variations in Nusselt number with $\Delta dp$ and $\Delta\varepsilon$ under $rp = 0.05$ m at $Re = 1305$.

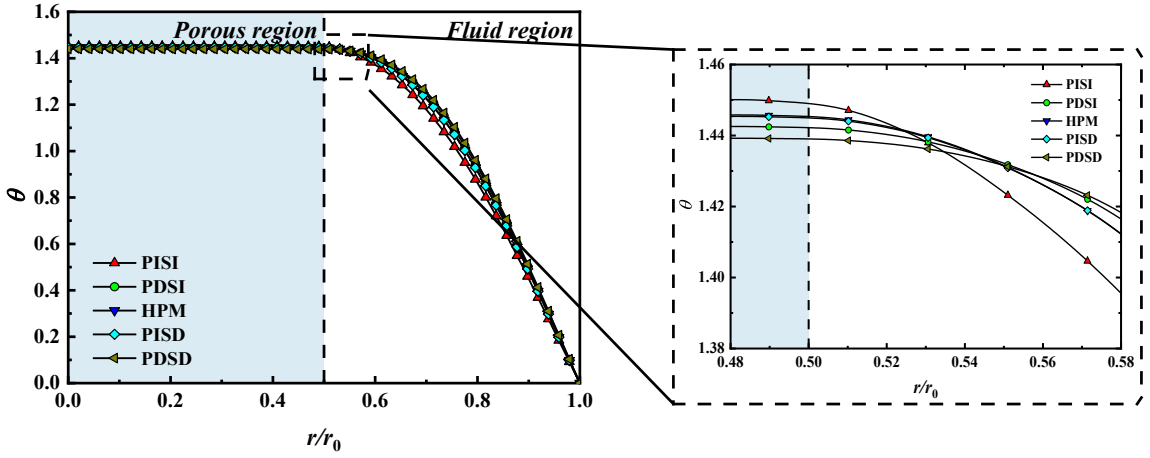


**Fig. 8.** Fully developed dimensionless temperature profiles along the radius direction of GPM and HPM with $rp/r0 = 0.5$ at $Re = 1305$.

### 3.3. Performance comparison with different filling ratio of GPM

Keeping the $\Delta dp$ and $\Delta\varepsilon$ of GPM as fixed values, the influence of the filling ratio ($r_d = r_p/r_0$) of GPM on the thermal-hydraulic performance is discussed in this section. Fig. 11 presents the velocity profiles of four configurations with different $r_d$. As shown in Fig. 11, the location corresponding to the maximum velocity is gradually increasing as the $r_d$ increases continuously, meanwhile, the maximum velocity is enhanced clarity and the increment of the maximum velocity for the $r_d$ from 0.5 to 0.7 is far larger than that from 0.3 to 0.5. Compared with the velocity profiles in the case of PISI, the velocity profiles near the axis of the tube are approximately coincident. This is attributed to the initial pore-sizes and porosities are the same as the different $r_d$. Along with the increase of the radius, the influence of $r_d$ leads to velocity differentiation, which is manifested as the higher the filling ratio is, the higher the velocity near the contact surface is. In contrast, the velocity in the porous region increases with the increasing $r_d$ in the other three configurations. In the case of PDSD, the increasing $r_d$ makes the velocity near the axis get a significant increase. In the whole porous region, the velocity of $r_d = 0.7$ is always higher than the others, and the velocity decreases finally to the minimum at the outermost porous region. In the case of PDSI and PISD, the velocities in the porous region changes slowly under the various $r_d$, which suddenly accelerates until in the clear fluid region. It indicates that no matter the filling ratio increases or decreases in the cases of PDSI and PISD, the effect of gradient under the same $\Delta dp$ and $\Delta\varepsilon$ is not obvious.

By comparing the temperature distribution curves of four configurations with different $r_d$ shown in Fig. 12, it can be seen that the thickness of the equivalent temperature boundary layer decreases gradually with the increasing $r_d$, and the isothermal area increases continuously. It is worth noting that the equivalent thermal conductivity of porous media differs greatly from that of air, so whether the $r_d$ increases or decreases, the effect of $\Delta dp$ and $\Delta\varepsilon$ on the isothermal region is unconsiderable. By comparing the dimensionless temperature of four configurations, it is not difficult to find that the more filling ratio $r_d$ is, the lower dimensionless temperature in the porous region is. Compared with the temperature reductions in the porous region caused by the increase of $r_d$, the reduction in PISI is the largest, while the variations of the other three cases are relatively close.

Fig. 13 and Fig. 14 show the influence of $\Delta dp$ and $\Delta\varepsilon$ on the $f$ and $Nu$ under different $r_d$. It can be seen that the trend of the $f$ and $Nu$ is quite similar, and both decrease with the increase of $\Delta dp$ and $\Delta\varepsilon$. Moreover, in the range of $\Delta dp < 0$ and $\Delta\varepsilon > 0$, the variations are obvious than that in other ranges. With the increasing $r_d$, both flow resistance and heat transfer performance are significantly enhanced, and the more $r_d$ increase, the more obvious the performance improvement is. Besides, the performance of GPM is more sensitive to the gradient under a larger $r_d$. Meanwhile, $\Delta dp$ has a stronger impact on performance than $\Delta\varepsilon$.

## 4. Optimization method and procedure

### 4.1. The optimization problem description

For the interests in the performance of GPM in this work, keeping

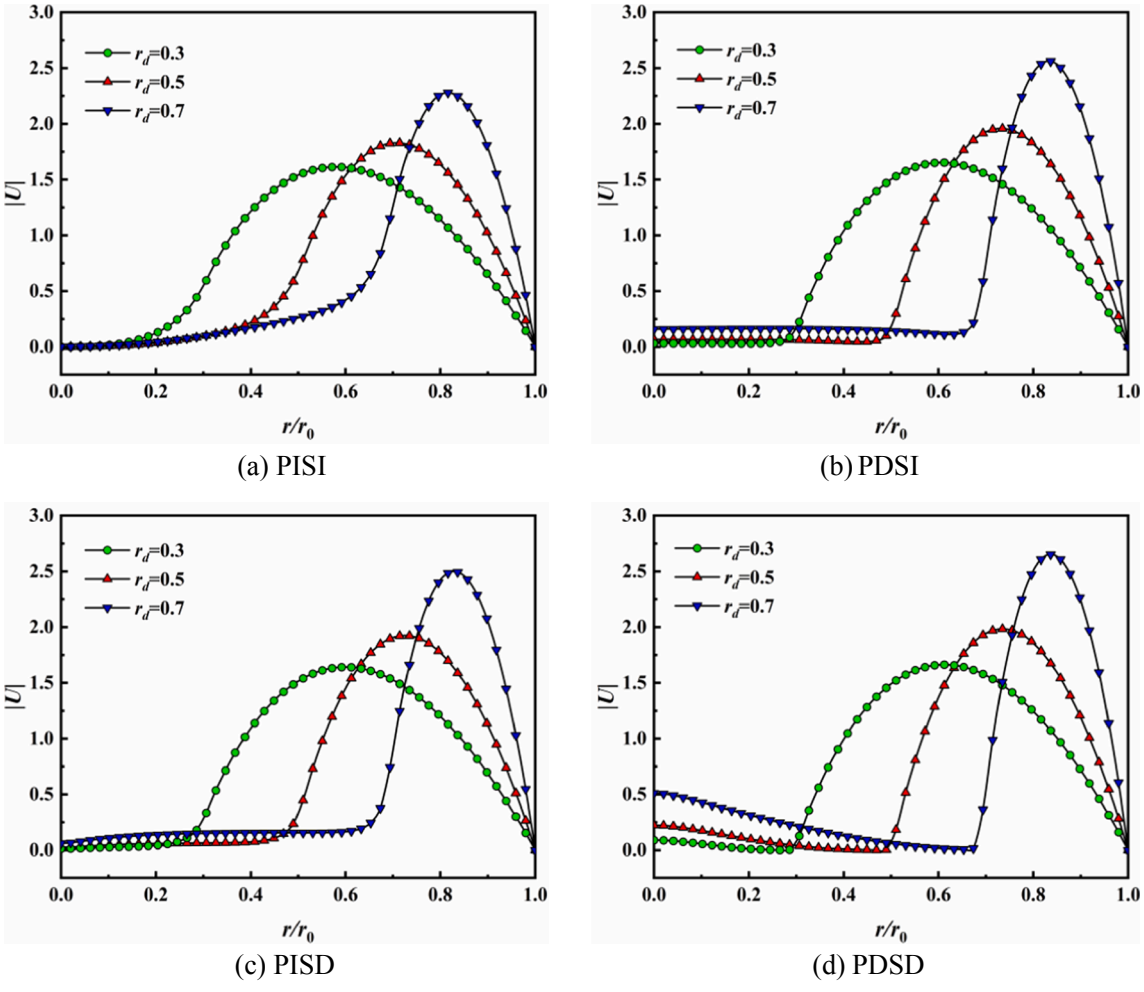


**Fig. 11.** Fully developed velocity profiles along the radius direction of four configurations of GPM under different filling ratio at $Re = 1305$.

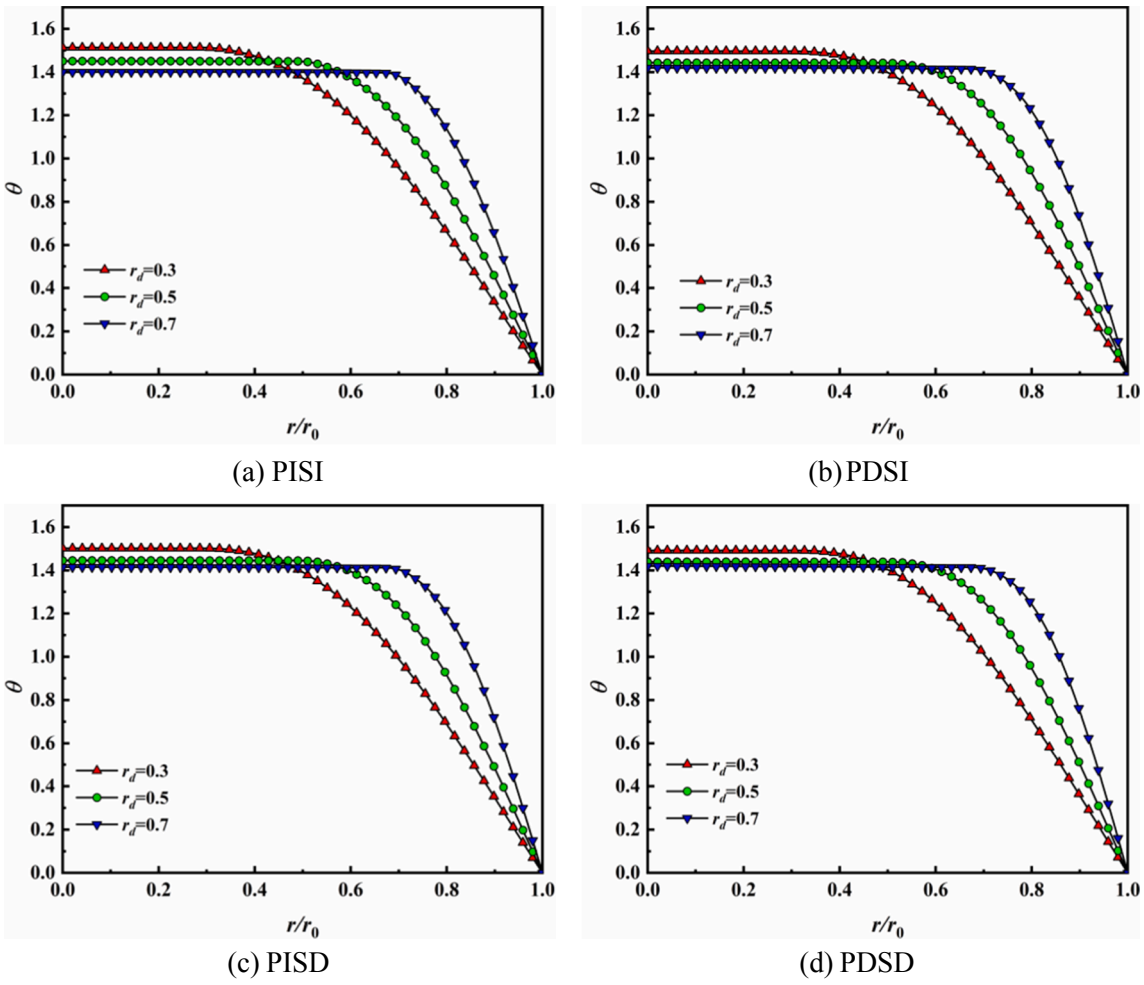


**Fig. 12.** Fully developed dimensionless temperature profiles along the radius direction of four configurations of GPM under different filling ratio at $Re = 1305$.

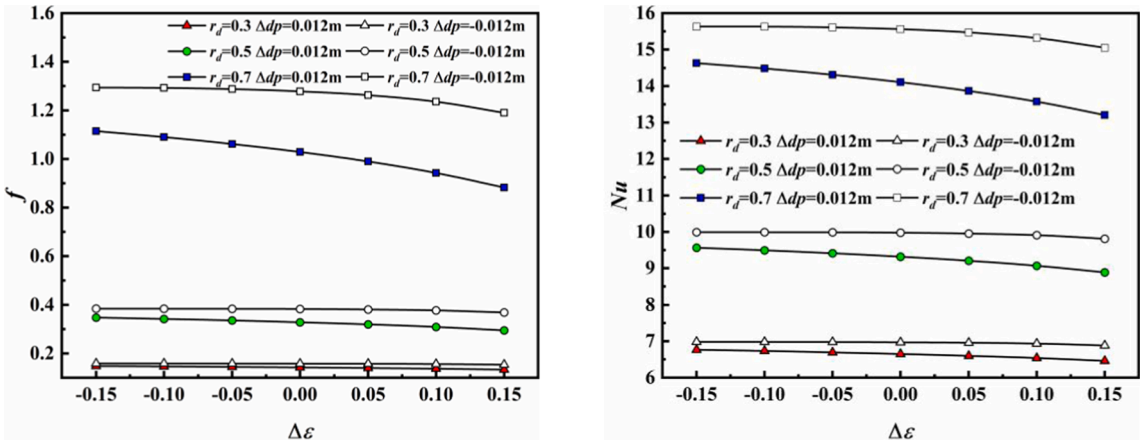


**Fig. 13.** Comparison of friction factor and Nusselt number with various $\Delta\varepsilon$ and $r_d$ under $\Delta dp = 0.012$ m or $\Delta dp = -0.012$ m.

other parameters as constant, a multi-objective optimization design is performed by employing $\Delta dp$ and $\Delta\varepsilon$ as design parameters, which considers the maximum heat transfer and the minimum flow resistance as the optimization objectives, hoping to get a more ideal preferential solution. The optimization problem can be described as:

$$\begin{gathered} find: X(\Delta dp, \Delta\varepsilon) \\ minimize: J_1 = f, and J_2 = -Nu \\ subjectto: -0.012 \leqslant \Delta dp \leqslant 0.012m, \ -0.15 \leqslant \Delta\varepsilon \leqslant 0.15 \end{gathered}$$

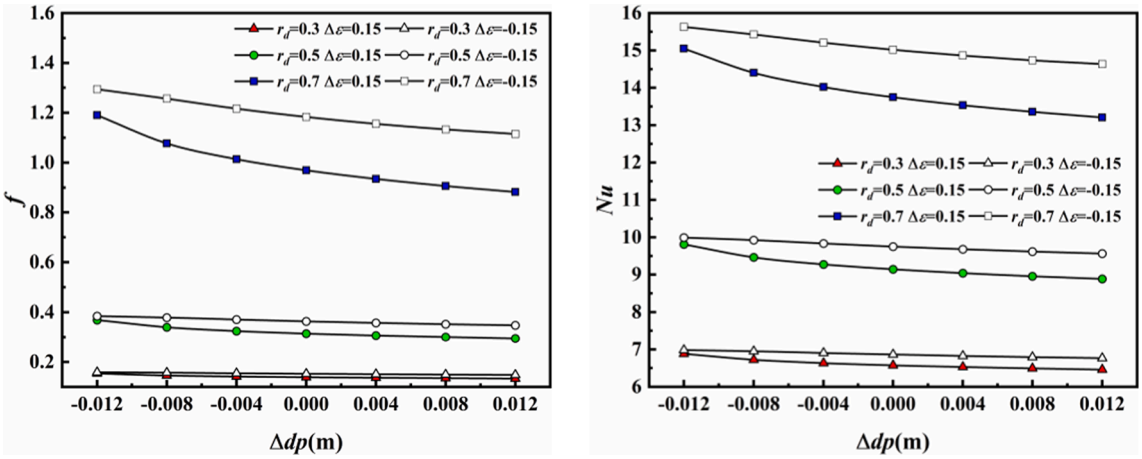


**(a)** Comparison of friction factor **(b)** Comparison of Nusselt number

**Fig. 14.** Comparison of friction factor and Nusselt number with various $\Delta dp$ and $r_d$ under $\Delta\varepsilon = 0.15$ or $\Delta\varepsilon = -0.15$.

### 4.2. Kriging model

The Kriging model is a widely used surrogate-model in engineering with the high accuracy and flexibility, which can give an unbiased estimate for all sample points [62,63]. According to the spatial location information and the degree of correlation between the observed points, different weights are assigned to different observation points for predicting the response of unobserved points. It is a semi-parametric interpolation technique, which consists of a regression part and a non-parametric part as [64]:

$$\widetilde{y}(x) = F(\gamma, x) + Z(x) \tag{21}$$

Where $F(\gamma, x)$ is the polynomial regression term which can be written as:

$$F(\gamma, x) = \gamma_1 f_1(x) + \gamma_2 f_2(x) + \cdots + \gamma_p f_p(x) = \sum_{i=1}^{p} \gamma_i f_i(x) \tag{22}$$

Where $\gamma$ is the regression coefficient, and $f(x)$ is the basis function, which can be taken as a constant or first-order or second-order polynomial function. $Z(x)$ is a random distribution function used to approximate local deviation, which has the following statistical characteristics:

$$\mathrm{Cov}\left[Z(x^i), Z(x^j)\right] = \sigma^2 R(\theta_k, x^i, x^j) \tag{23}$$

Here, $R(\theta, x^i, x^j)$ represents the correlation function between any two sample points, and $\theta$ is the relevant parameter. For different engineering problems, the correlation functions used are also different. In this paper, the correlation function is:

$$R(\theta_k, x^i, x^j) = exp\left[-\sum_{k=1}^{N} \theta_k \left| x_k^i - x_k^j \right|\right] \tag{24}$$

As the sample set $[X_{N\times n}|\ X_{N\times 1}]$, the response value $\widetilde{y}(x)$ at the point $x$ can be estimated according to the Kriging model:

$$\widetilde{y}(x) = f(x)^T \gamma + r(x)^T R^{-1}(Y - y\gamma) \tag{25}$$

Where:

$$R = \begin{bmatrix} R(x^1, x^1) & R(x^1, x^2) & \cdots & R(x^1, x^N) \\ R(x^2, x^1) & R(x^2, x^2) & \cdots & R(x^2, x^N) \\ \vdots & \vdots & \vdots & \vdots \\ R(x^N, x^1) & R(x^N, x^2) & \cdots & R(x^N, x^N) \end{bmatrix} \tag{26}$$

$$\gamma = \left[\gamma_1, \gamma_2, \gamma_3, \cdots, \gamma_p\right]^T \tag{27}$$

$$f(x) = \left[f_1(x), f_2(x), \cdots, f_p(x)\right]^T \tag{28}$$

$$y = \left[f(x^1)^T, f(x^2)^T, \cdots, f(x^N)^T\right]^T \tag{29}$$

$$r(x) = \left[R(x, x^1), R(x, x^2), \cdots, R(x, x^N)\right]^T \tag{30}$$

According to the predicted optimal linear unbiased estimation, the undetermined coefficients $\gamma$ can be obtained:

$$\gamma = \left(y^T R^{-1} y\right)^{-1} y^T R^{-1} Y \tag{31}$$

According to the maximum likelihood estimation method, $\theta_k$ is calculated by solving the unconstrained optimization problem:

$$\max_{\theta_k > 0}\left[-\frac{1}{2}\left(N ln\sigma^2 + ln|R|\right)\right] \tag{32}$$

The variance $\sigma^2$ can be expressed as:

$$\sigma^2 = \frac{1}{N}(Y - y\gamma)^T R^{-1}(Y - y\gamma) \tag{33}$$

### 4.3. Multi-objective optimization

For the problem of multiple optimization objectives in the optimization process, a multi-objective genetic optimization algorithm (MOGA) can be used to accurately and effectively solve the problem [65–68]. The NSGA-II algorithm employed in this paper is developed and established by the researcher Deb [69] based on the non-dominated sorting genetic algorithm. Compared with other evolutionary strategies, the algorithm has good search performance and is suitable for contradictory and extensive targets. The specific steps for the NSGA-II algorithm are described in detail as Fig. 15, and the genetic algorithm parameters are shown in Table 2.

**Step 1:** Generate randomly an initial population $P_t$ of size $N$;
**Step 2:** Product an offspring population $Q_t$ by performing genetic operators and combine $P_t$ with $Q_t$ to generate a new population $R_t$ of size 2 $N$;
**Step 3:** Rank all individuals in the population $R_t$ by non-dominated sorting and further calculate the crowding distance if individuals have same rank, and then select suitable individuals until obtaining the next population $P_{t+1}$ of size $N$;
**Step 4:** identify the termination conditions, and perform the above steps until the termination conditions are satisfied.
**Dominance relation:** An individual X1 dominated an individual X2 can be described as satisfying any of the following conditions:
(a) X1 is no worse than X2 in all objectives;

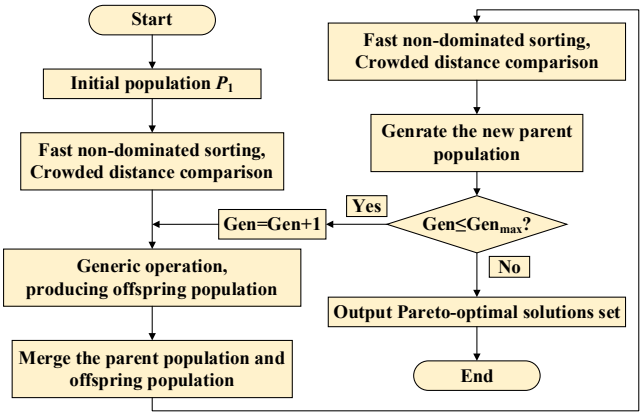


**Fig. 15.** Flow chart of NSGA-II optimization.

**Table 2**
Parameters of NSGA-II.

| Parameters | Value |
|---|---|
| Population size | 350 |
| Crossover fraction | 0.85 |
| Mutation fraction | 0.2 |
| Pareto front population fraction | 0.4 |
| Generations | 200 |

(b) X1 is strictly better than X2 in at least one objective.

**Crowding distance:** Crowding distance is used to sort individuals under the same non-dominant rank, which is calculated as follows:

$$I[i]_d = \begin{Bmatrix} \infty, \ i = 1, l \\ I[i]_d + \dfrac{I[i+1]_m - I[i-1]_m}{f_m^{max} - f_m^{min}}, \ i = 2, 3, \ldots, l-1 \end{Bmatrix}$$

where $I[i]_d$ denotes the crowding distance of the $i$-th individual, $I[i+1]_m$ represents the $m$-th objective value of the $i+1$-th individual, and $f_m^{max}$ and $f_m^{min}$ are the maximum and minimum values of the $m$-th objective function, respectively.

### 4.4. Optimization procedure

The framework of the optimization procedure combined with the Kriging model and MOGA is mainly comprised of five components as shown in Fig. 16: identify the optimization goals and design parameters, design of experiment, numerical solution, construct surrogate model, and multi-objective optimization. As discussed previously, $\Delta dp$ and $\Delta\varepsilon$ are selected as design parameters aimed to explore the optimal variable distribution weighed the flow and heat transfer performance. Subsequently, the experiment needs to be designed to obtain the observation points for constructing the Kriging model. Since the accuracy of the optimization results is greatly affected by the fitting effect of the surrogate model, considering the small dimensions of the design variables, the full-factor experiment is employed that $7 \times 7$ experimental points are uniformly sampled in the variable space and are numerically calculated by the CFD software to obtain the corresponding results. With the sampled data, the Kriging model can be constructed by seeking the $\theta_k$ listed in equation (32). Fig. 17 shows the schematic diagram of the constructed Kriging model. The red points are the experimental data obtained by numerical calculation and the response surface is built by the predictor of the constructed Kriging model. And as depicted in Fig. 17, the sample points fit well with the response surface, which proves the accuracy of the kriging model established in this work. Lastly, the NSGA-II algorithm is utilized to seek the candidate solutions in-terms of both objectives.

## 5. Optimization results and discussion

The gradients of GPM are optimized by the multi-objective genetic algorithm under the various filling ratio $r_d$, and then the Pareto solutions are obtained as shown in Fig. 18. It can be seen from the figure that there is a clear conflict between the thermal and hydraulic performance, the

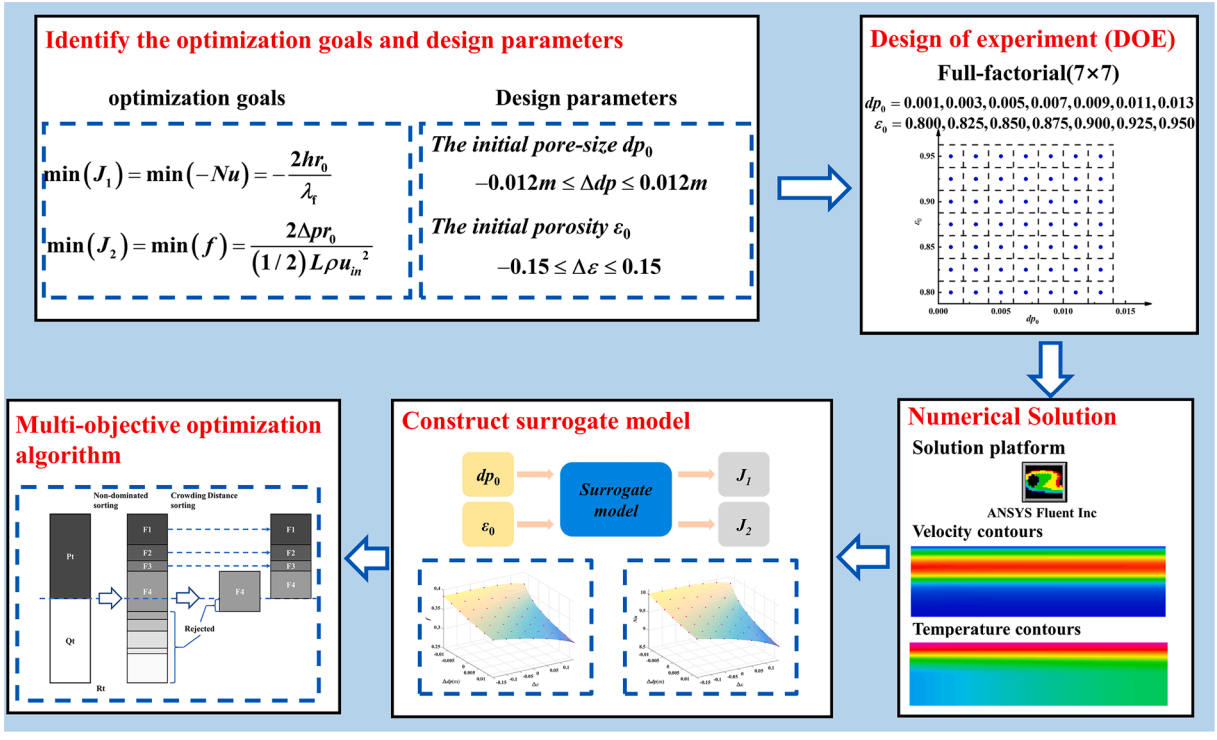


**Fig. 16.** A framework for optimizing $\Delta dp$ and $\Delta\varepsilon$ based Kriging model and genetic algorithm.

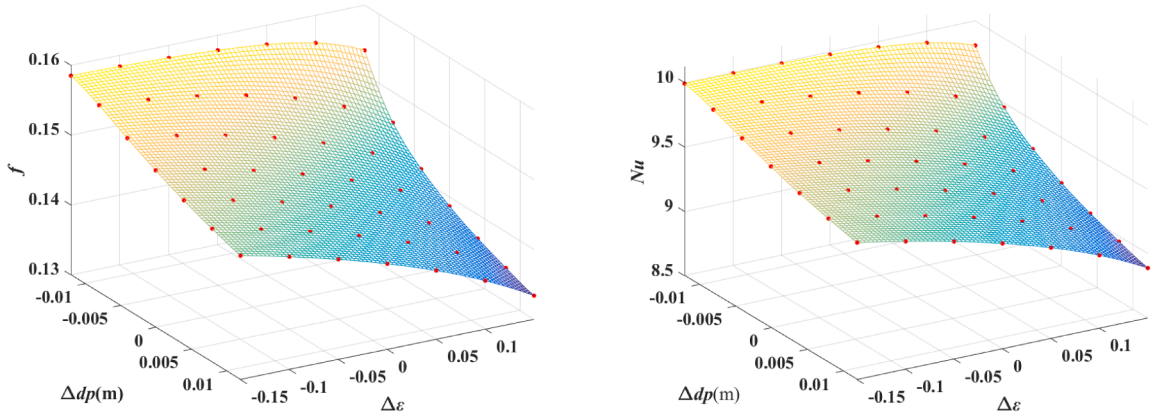


(a) $r_d$=0.3

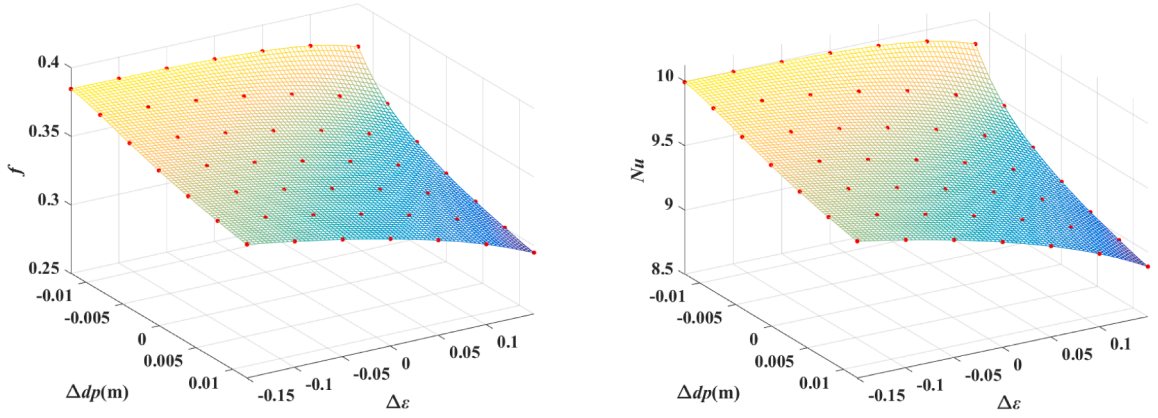


(b) $r_d$ =0.5

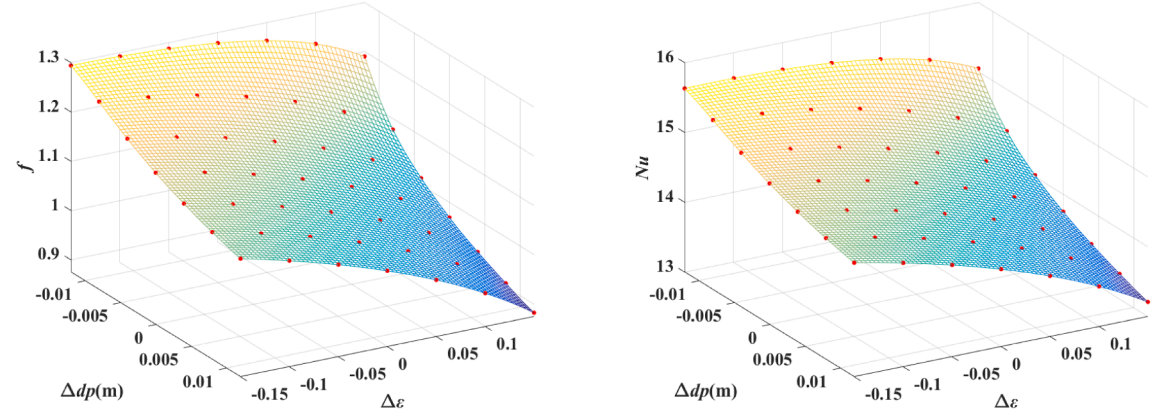


(c) $r_d$ =0.7

**Fig. 17.** Comparison of the predicted and observed values.

enhancement of heat transfer is at the cost of increasing the flow resistance. The Pareto solutions shown in the figure present a linear distribution. The expressions of the fitting lines are different under different $r_d$. In the case of $r_d = 0.3$, the relationship between two objectives, the flow resistance $J_1$ and the heat transfer performance $J_2$ can be expressed by the linear equation: $J_2 = -20.80208 \times J_1 - 3.69062$. Within the limited variation range of variables, the maximum $Nu = 6.9837$ is 3.271% larger than that of HPM and the minimum $f = 0.1334$ is 9.624% smaller than that of HPM. In the case of $r_d = 0.5$, the relationship between the two objectives can be expressed by the linear equation: $J_2 = -12.39332 \times J_1 - 5.24763$, the absolute value of the slope decreases compared with $r_d = 0.3$, while the variation range of the optimal $f$ and $Nu$ increases obviously. In the case of $r_d = 0.7$, the relationship between the two objectives can be expressed by the linear equation: $J_2 =$

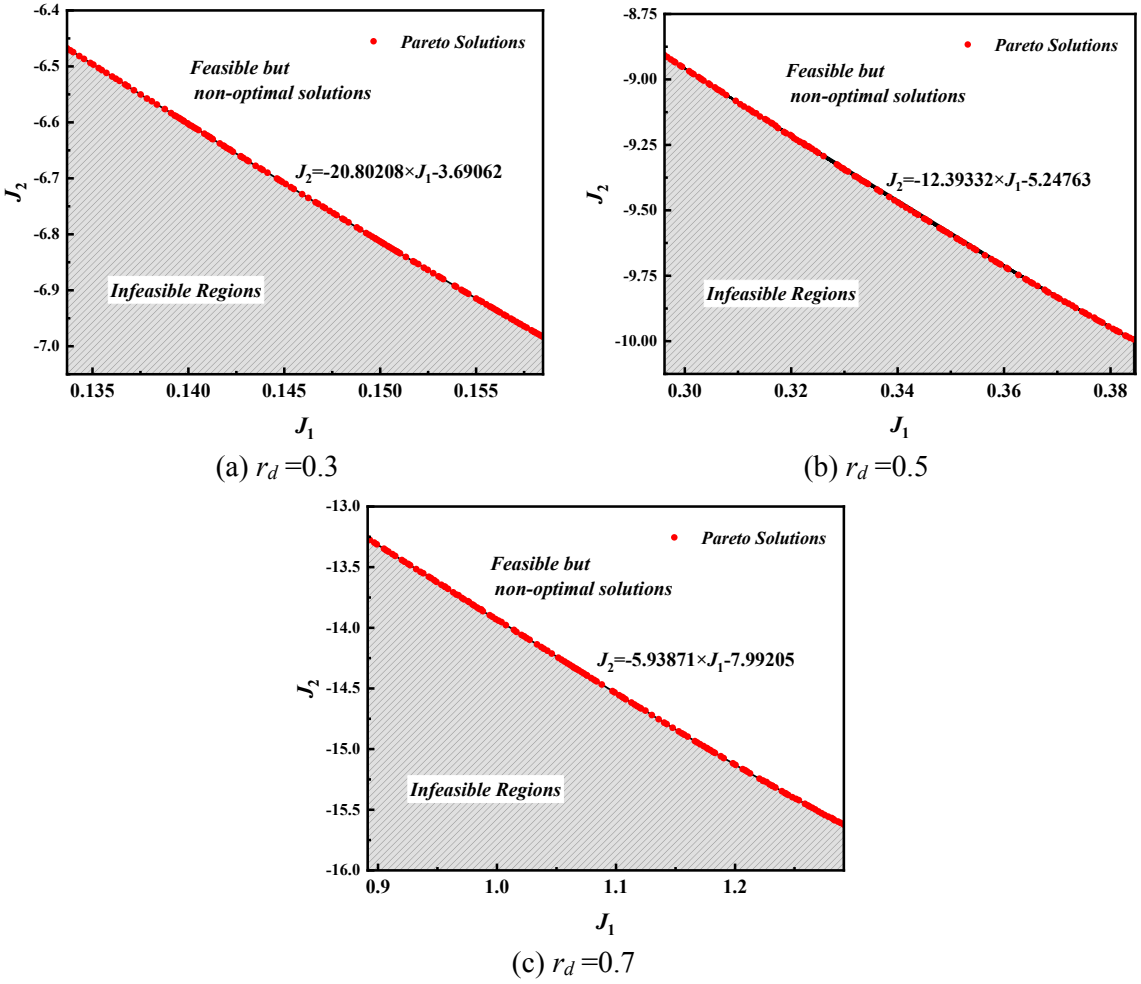


**Fig. 18.** Pareto solutions plot for $J_1$ and $J_2$.

$-5.93871 \times J_1 - 7.99205$. The absolute value of the slope is further reduced, but the variation range of *Nu* and *f* is further expanded. The flow resistance can be reduced by up to 19.573%, and the heat transfer efficiency can be increased by up to 7.088% compared with the homogeneous porous media.

Fig. 19 shows the spatial distribution of the design variables corresponding to the optimal Pareto solution. As shown in the figure, the distributions of the optimal design variables under different *rp* are quite similar, and the variation range of optimal design variables is as same as the design space, indicating that the flow and heat transfer performance keep in conflict in the entire design space. A large number of optimal points are distributed in PDSD, PISD, and PISI, and only a small number of points are distributed in PDSI. It can be seen that both the flow and heat transfer performances of PDSI are not prominent compared with the other configurations.

## 6. Conclusion

The present paper mainly investigates the combined effects of the gradients of gradient porous media on thermal and hydraulic performance. Four different configurations combined with the different gradients of pore-size and porosity are formed and compared with homogeneous porous media. The optimal configurations, including minimum flow resistance, maximum heat transfer, and different weights of the two performances are obtained by parametric analysis and multi-objective optimization. The conclusions can be drawn as follows:

1. The configuration where porosity and pore-size increase simultaneously along the radius has the best heat transfer performance, while a simultaneous decrease has the minimum flow resistance. The configuration with the increasing pore-size and decreasing porosity have a similar performance with the homogeneous porous media.
2. For a given pore-size gradient, both the friction factor and the Nusselt number decrease with the increasing porosity gradient, and the variation get inconsiderable as the pore-size gradient decreases.
3. With the increasing filling ratio $r_d$, both flow resistance and heat transfer efficiency are significantly enhanced, and the sensitivity of both to the gradient variations is also increased.
4. The optimization results present linear distribution between the two objectives, and the slope of the fitting line decreases with the increase of the filling ratio. The configuration with the decreasing pore-size and increasing porosity is not outstanding in both flow and heat transfer performance.

## CRediT authorship contribution statement

**Chunyu Shi:** Conceptualization, Methodology, Software, Validation, Formal analysis, Investigation, Data curation. **Miaozhi Wang:** Methodology, Software, Data curation. **Jun Yang:** Methodology, Software. **Wei Liu:** Resources, Supervision, Project administration, Funding acquisition. **Zhichun Liu:** Conceptualization, Resources, Supervision, Project administration, Funding acquisition.

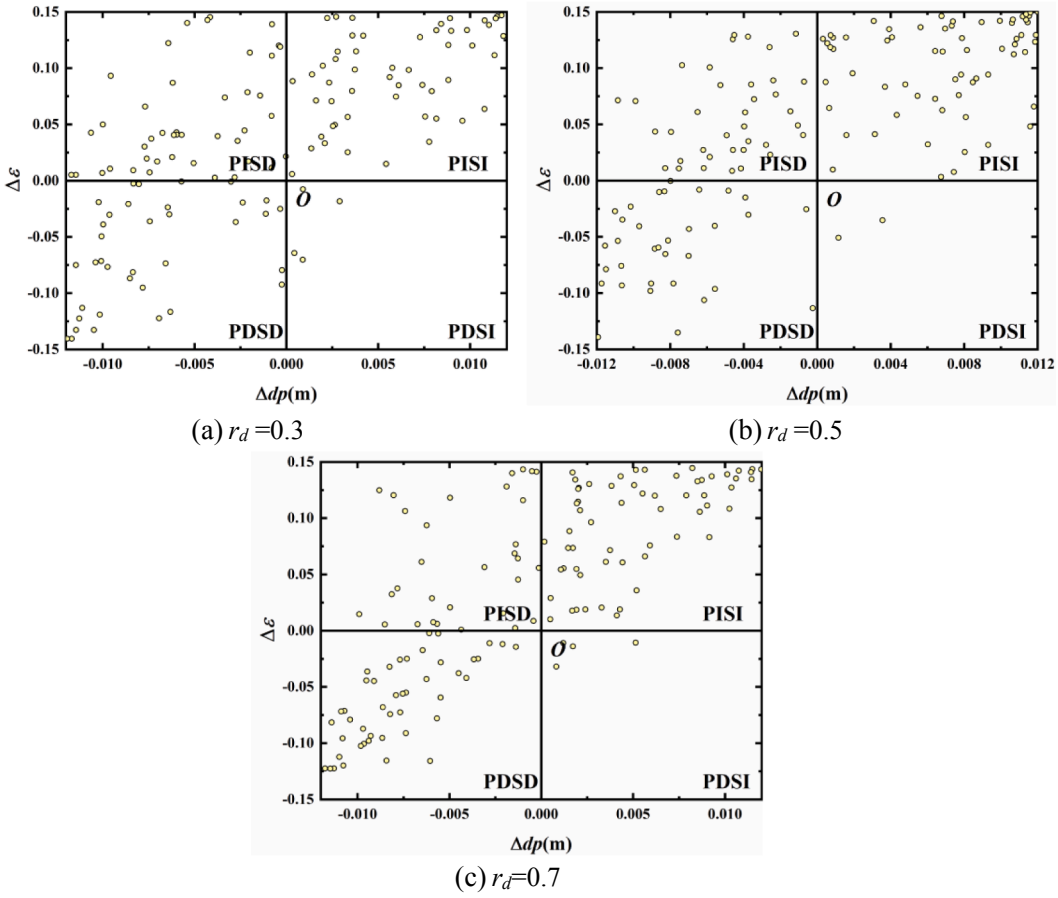


**Fig. 19.** Distributions of $\Delta dp$ and $\Delta\varepsilon$ corresponding to the Pareto solutions.

## Declaration of Competing Interest

The authors have declared that no conflict of interest exists.

## Acknowledgment

This work is Supported by the National Natural Science Foundation of China (No. 51736004 & 51776079) and the Foundation of State Key Laboratory of Coal Combustion (FSKLCCA2007).

## References

[1] W.-Q. Tao, Z.-Y. Guo, B.-X. Wang, Field synergy principle for enhancing convective heat transfer—its extension and numerical verifications, Int. J. Heat Mass Transf. 45 (18) (2002) 3849–3856.
[2] C.K. Mangrulkar, A.S. Dhoble, A.R. Deshmukh, S.A. Mandavgane, Numerical investigation of heat transfer and friction factor characteristics from in-line cam shaped tube bank in crossflow, Appl. Therm. Eng. 110 (2017) 521–538. 10.1016/j.applthermaleng.2016.08.174.
[3] M. Akhbari, A. Rahimi, M.S. Hatamipour, Modeling and experimental study of a triangular channel solar air heater, Appl. Therm. Eng. 170 (2020) 114902, https://doi.org/10.1016/j.applthermaleng.2020.114902.
[4] M.H. Cheraghi, M. Ameri, M. Shahabadi, Numerical study on the heat transfer enhancement and pressure drop inside deep dimpled tubes, Int. J. Heat Mass Transf. 147 (2020) 118845, https://doi.org/10.1016/j.ijheatmasstransfer.2019.118845.
[5] M. Dastmalchi, G.A. Sheikhzadeh, A. Arefmanesh, Optimization of micro-finned tubes in double pipe heat exchangers using particle swarm algorithm, Appl. Therm. Eng. 119 (2017) 1–9. 10.1016/j.applthermaleng.2017.03.025.
[6] S. Huang, Z. Wan, Y. Tang, Manufacturing and single-phase thermal performance of an arc-shaped inner finned tube for heat exchanger, Appl. Therm. Eng. 159 (2019) 113817, https://doi.org/10.1016/j.applthermaleng.2019.113817.
[7] S. Chamoli, R. Lu, J. Xie, P. Yu, Numerical study on flow structure and heat transfer in a circular tube integrated with novel anchor shaped inserts, Appl. Therm. Eng. 135 (2018) 304–324. 10.1016/j.applthermaleng.2018.02.052.
[8] M.E. Nakhchi, J.A. Esfahani, Numerical investigation of different geometrical parameters of perforated conical rings on flow structure and heat transfer in heat exchangers, Appl. Therm. Eng. 156 (2019) 494–505. 10.1016/j.applthermaleng.2019.04.067.
[9] F.A.S. da Silva, D.J. Dezan, A.V. Pantaleão, L.O. Salviano, Longitudinal vortex generator applied to heat transfer enhancement of a flat plate solar water heater, Appl. Therm. Eng. 158 (2019) 113790, https://doi.org/10.1016/j.applthermaleng.2019.113790.
[10] Y. Wang, P. Liu, F. Shan, Z. Liu, W. Liu, Effect of longitudinal vortex generator on the heat transfer enhancement of a circular tube, Appl. Therm. Eng. 148 (2019) 1018–1028, https://doi.org/10.1016/j.applthermaleng.2018.11.080.
[11] J. Banhart, Manufacture, characterisation and application of cellular metals and metal foams, Prog. Mater Sci. 46 (6) (2001) 559–632.
[12] H. Duan, X. Shen, Q. Yin, F. Yang, P. Bai, X. Zhang, M. Pan, Modeling and optimization of sound absorption coefficient of microperforated compressed porous metal panel absorber, Appl. Acoust. 166 (2020) 107322, https://doi.org/10.1016/j.apacoust.2020.107322.
[13] T. Wan, Y. Liu, C. Zhou, X. Chen, Y. Li, Fabrication, properties, and applications of open-cell aluminum foams: A review, J. Mater. Sci. Technol. 62 (2021) 11–24.
[14] Y. Xu, Q. Ren, Z.-J. Zheng, Y.-L. He, Evaluation and optimization of melting performance for a latent heat thermal energy storage unit partially filled with porous media, Appl. Energy 193 (2017) 84–95.
[15] M.M. Heyhat, S. Mousavi, M. Siavashi, Battery thermal management with thermal energy storage composites of PCM, metal foam, fin and nanoparticle, J. Storage Mater. 28 (2020) 101235, https://doi.org/10.1016/j.est.2020.101235.
[16] X. Yang, J. Yu, Z. Guo, L. Jin, Y.-L. He, Role of porous metal foam on the heat transfer enhancement for a thermal energy storage tube, Appl. Energy 239 (2019) 142–156.
[17] H. Pourrahmani, M. Moghimi, M. Siavashi, M. Shirbani, Sensitivity analysis and performance evaluation of the PEMFC using wave-like porous ribs, Appl. Therm. Eng. 150 (2019) 433–444.
[18] A. Izadi, M. Siavashi, H. Rasam, Q. Xiong, MHD enhanced nanofluid mediated heat transfer in porous metal for CPU cooling, Appl. Therm. Eng. 168 (2020) 114843, https://doi.org/10.1016/j.applthermaleng.2019.114843.
[19] F. Selimefendigil, F. Bayrak, H.F. Oztop, Experimental analysis and dynamic modeling of a photovoltaic module with porous fins, Renewable Energy 125 (2018) 193–205.
[20] T. Wang, W. Luan, T. Liu, S.-T. Tu, J. Yan, Performance enhancement of thermoelectric waste heat recovery system by using metal foam inserts, Energy Convers. Manage. 124 (2016) 13–19.

[21] Y. Li, S. Wang, Y. Zhao, C. Lu, Experimental study on the influence of porous foam metal filled in the core flow region on the performance of thermoelectric generators, Appl. Energy 207 (2017) 634–642.
[22] A.A. Mohamad, Heat transfer enhancements in heat exchangers fitted with porous media Part I: constant wall temperature, Int. J. Therm. Sci. 42 (4) (2003) 385–395.
[23] S. Mahjoob, K. Vafai, A synthesis of fluid and thermal transport models for metal foam heat exchangers, Int. J. Heat Mass Transf. 51 (15-16) (2008) 3701–3711.
[24] Y.-T. Yang, M.-L. Hwang, Numerical simulation of turbulent fluid flow and heat transfer characteristics in heat exchangers fitted with porous media, Int. J. Heat Mass Transf. 52 (13-14) (2009) 2956–2965.
[25] Z.F. Huang, A. Nakayama, K. Yang, C. Yang, W. Liu, Enhancing heat transfer in the core flow by using porous medium insert in a tube, Int. J. Heat Mass Transf. 53 (5-6) (2010) 1164–1174.
[26] M.A. Teamah, W.M. El-Maghlany, M.M. Khairat Dawood, Numerical simulation of laminar forced convection in horizontal pipe partially or completely filled with porous material, Int. J. Therm. Sci. 50 (8) (2011) 1512–1522.
[27] Y.a. Ge, Z. Liu, W. Liu, Multi-objective genetic optimization of the heat transfer for tube inserted with porous media, Int. J. Heat Mass Transf. 101 (2016) 981–987.
[28] M. Siavashi, H.R. Talesh Bahrami, H. Saffari, Numerical investigation of flow characteristics, heat transfer and entropy generation of nanofluid flow inside an annular pipe partially or completely filled with porous media using two-phase mixture model, Energy 93 (2015) 2451–2466.
[29] M. Siavashi, H.R.T. Bahrami, H. Saffari, Numerical investigation of porous rib arrangement on heat transfer and entropy generation of nanofluid flow in an annulus using a two-phase mixture model, Numer. Heat Transfer, Part A: Appl. 71 (12) (2017) 1251–1273.
[30] P.-C. Huang, C.-C. Chen, Simulation of mixed convection in a vertical channel containing discrete porous-covering heat blocks, Int. J. Heat Mass Transf. 55 (11-12) (2012) 3147–3159.
[31] T.-C. Hung, Y.-X. Huang, W.-M. Yan, Thermal performance of porous microchannel heat sink: Effects of enlarging channel outlet, Int. Commun. Heat Mass Transfer 48 (2013) 86–92.
[32] T.-C. Hung, Y.-X. Huang, W.-M. Yan, Thermal performance analysis of porous-microchannel heat sinks with different configuration designs, Int. J. Heat Mass Transf. 66 (2013) 235–243.
[33] T.-C. Hung, W.-M. Yan, Optimization of Design Parameters for a Sandwich-Distribution Porous-Microchannel Heat Sink, Numer. Heat Transfer, Part A: Appl. 66 (3) (2014) 229–251.
[34] T.-C. Hung, Y.-X. Huang, T.-S. Sheu, W.-M. Yan, Numerical Optimization of the Thermal Performance of a Porous-Microchannel Heat Sink, Numer. Heat Transfer, Part A: Appl. 65 (5) (2014) 419–434.
[35] B. Shen, H. Yan, B. Sunden, H. Xue, G. Xie, Forced convection and heat transfer of water-cooled microchannel heat sinks with various structured metal foams, Int. J. Heat Mass Transf. 113 (2017) 1043–1053.
[36] Y.P. Du, Z.G. Qu, C.Y. Zhao, W.Q. Tao, Numerical study of conjugated heat transfer in metal foam filled double-pipe, Int. J. Heat Mass Transf. 53 (21-22) (2010) 4899–4907.
[37] N. Targui, H. Kahalerras, Analysis of a double pipe heat exchanger performance by use of porous baffles and pulsating flow, Energy Convers. Manage. 76 (2013) 43–54.
[38] K. Milani Shirvan, R. Ellahi, S. Mirzakhanlari, M. Mamourian, Enhancement of heat transfer and heat exchanger effectiveness in a double pipe heat exchanger filled with porous media: Numerical simulation and sensitivity analysis of turbulent fluid flow, Appl. Therm. Eng. 109 (2016) 761–774.
[39] K. Milani Shirvan, S. Mirzakhanlari, S.A. Kalogirou, H.F. Öztop, M. Mamourian, Heat transfer and sensitivity analysis in a double pipe heat exchanger filled with porous medium, Int. J. Therm. Sci. 121 (2017) 124–137.
[40] A. Alhusseny, A. Turan, A. Nasser, Rotating metal foam structures for performance enhancement of double-pipe heat exchangers, Int. J. Heat Mass Transf. 105 (2017) 124–139.
[41] M. Siavashi, S.M. Miri Joibary, Numerical performance analysis of a counter-flow double-pipe heat exchanger with using nanofluid and both sides partly filled with porous media, J. Therm. Anal. Calorim. 135 (2) (2019) 1595–1610.
[42] S.M. Miri Joibary, M. Siavashi, Effect of Reynolds asymmetry and use of porous media in the counterflow double-pipe heat exchanger for passive heat transfer enhancement, J. Therm. Anal. Calorim. 140 (3) (2020) 1079–1093.
[43] R. Nazar, L. Tham, I. Pop, D.B. Ingham, Mixed Convection Boundary Layer Flow from a Horizontal Circular Cylinder Embedded in a Porous Medium Filled with a Nanofluid, Transp. Porous Med. 86 (2) (2011) 517–536.
[44] A.M. Rashad, A.J. Chamkha, M. Modather, Mixed convection boundary-layer flow past a horizontal circular cylinder embedded in a porous medium filled with a nanofluid under convective boundary condition, Comput. Fluids 86 (2013) 380–388.
[45] M. Siavashi, S. Iranmehr, Using sharp wedge-shaped porous media in front and wake regions of external nanofluid flow over a bundle of cylinders, HFF 29 (10) (2019) 3730–3755.
[46] M. Siavashi, R. Yousofvand, S. Rezanejad, Nanofluid and porous fins effect on natural convection and entropy generation of flow inside a cavity, Adv. Powder Technol. 29 (1) (2018) 142–156.
[47] K. Ghasemi, M. Siavashi, MHD nanofluid free convection and entropy generation in porous enclosures with different conductivity ratios, J. Magn. Magn. Mater. 442 (2017) 474–490.
[48] L.E. Murr, S.M. Gaytan, D.A. Ramirez, E. Martinez, J. Hernandez, K.N. Amato, P. W. Shindo, F.R. Medina, R.B. Wicker, Metal Fabrication by Additive Manufacturing Using Laser and Electron Beam Melting Technologies, J. Mater. Sci. Technol. 28 (1) (2012) 1–14.
[49] X. Yang, P. Wei, X. Wang, Y.-L. He, Gradient design of pore parameters on the melting process in a thermal energy storage unit filled with open-cell metal foam, Appl. Energy 268 (2020) 115019, https://doi.org/10.1016/j.apenergy.2020.115019.
[50] S. Asiaei, A. Zadehkafi, M. Siavashi, Multi-layered Porous Foam Effects on Heat Transfer and Entropy Generation of Nanofluid Mixed Convection Inside a Two-Sided Lid-Driven Enclosure with Internal Heating, Transp. Porous Med. 126 (1) (2019) 223–247.
[51] P. Maghsoudi, M. Siavashi, Application of nanofluid and optimization of pore size arrangement of heterogeneous porous media to enhance mixed convection inside a two-sided lid-driven cavity, J. Therm. Anal. Calorim. 135 (2) (2019) 947–961.
[52] M. Tahmasbi, M. Siavashi, H.R. Abbasi, M. Akhlaghi, Mixed convection enhancement by using optimized porous media and nanofluid in a cavity with two rotating cylinders, J. Therm. Anal. Calorim. 141 (5) (2020) 1829–1846.
[53] Z.-J. Zheng, M.-J. Li, Y.-L. He, Optimization of porous insert configurations for heat transfer enhancement in tubes based on genetic algorithm and CFD, Int. J. Heat Mass Transf. 87 (2015) 376–379.
[54] B. Wang, Y. Hong, X. Hou, Z. Xu, P. Wang, X. Fang, X. Ruan, Numerical configuration design and investigation of heat transfer enhancement in pipes filled with gradient porous materials, Energy Convers. Manage. 105 (2015) 206–215.
[55] B. Wang, Y. Hong, L. Wang, X. Fang, P. Wang, Z. Xu, Development and numerical investigation of novel gradient-porous heat sinks, Energy Convers. Manage. 106 (2015) 1370–1378.
[56] M. Siavashi, H.R. Talesh Bahrami, E. Aminian, Optimization of heat transfer enhancement and pumping power of a heat exchanger tube using nanofluid with gradient and multi-layered porous foams, Appl. Therm. Eng. 138 (2018) 465–474.
[57] D.A. Nield, A. Bejan (Eds.), Convection in Porous Media, Springer, New York, NY, 2013, https://doi.org/10.1007/978-1-4614-5541-7.
[58] S. Ergun, Fluid flow through packed columns, Chem. Eng. Prog. (1952).
[59] M. Kaviany, Principles of Heat Transfer in Porous Media, Mech. Eng. Ser. (1995).
[60] J.R. Welty, C.E. Wicks, R.E. Wilson, Fundamentals of momentum, heat, and mass transfer, third ed. (1984).
[61] B.I. Pavel, A.A. Mohamad, An experimental and numerical study on heat transfer enhancement for gas heat exchangers fitted with porous media, Int. J. Heat Mass Transf. 47 (23) (2004) 4939–4952.
[62] P. Lu, J. Pan, T. Hong, D. Li, Y. Chen, Prediction method of bridge static deformation based on dynamic test, Struct. Concr. 21 (6) (2020) 2533–2548.
[63] D.a. Cui, G. Wang, Y. Lu, K. Sun, Reliability design and optimization of the planetary gear by a GA based on the DEM and Kriging model, Reliab. Eng. Syst. Saf. 203 (2020) 107074, https://doi.org/10.1016/j.ress.2020.107074.
[64] X.i. Li, Y. Li, H. Zhu, S. Deng, An effective operating parameters optimization method for electrowinning process of zinc based on kriging model and finite element model, IFAC-PapersOnLine 51 (21) (2018) 70–75.
[65] Y. Ge, F. Shan, Z. Liu, W. Liu, Optimal Structural Design of a Heat Sink With Laminar Single-Phase Flow Using Computational Fluid Dynamics-Based Multi-Objective Genetic Algorithm, J. Heat Transfer. 140 (2018). https://doi.org/10.1115/1.4037643.
[66] S. Sanaye, H. Hajabdollahi, Thermal-economic multi-objective optimization of plate fin heat exchanger using genetic algorithm, Appl. Energy 87 (6) (2010) 1893–1902.
[67] Z. Liu, X. Zeng, Y.a. Ge, J. Shen, W. Liu, Multi-objective optimization of operating conditions and channel structure for a proton exchange membrane fuel cell, Int. J. Heat Mass Transf. 111 (2017) 289–298.
[68] H. Han, R. Yu, B. Li, Y. Zhang, Multi-objective optimization of corrugated tube inserted with multi-channel twisted tape using RSM and NSGA-II, Appl. Therm. Eng. 159 (2019) 113731, https://doi.org/10.1016/j.applthermaleng.2019.113731.
[69] K. Deb, A. Pratap, S. Agarwal, T. Meyarivan, A fast and elitist multiobjective genetic algorithm: NSGA-II, IEEE Trans. Evol. Comput. (2002). https://doi.org/10.1109/4235.996017.